Structural and optical behaviors of 2D-layered molybdenum disulfide thin film

Barakat, F.; Laref, A.; Alterary, S.; Faraji, S.; Alsalhi, M.

Published in:
Journal of Materials Research and Technology

DOI:
10.1016/j.jmrt.2021.06.059

Publication date:
2021

Available online at www.sciencedirect.com

jmr&t Journal of Materials Research and Technology

journal homepage: www.elsevier.com/locate/jmrt

Original Article

Structural and optical behaviors of 2D-layered molybdenum disulfide thin film: experimental and ab-initio insights

F. Barakat [a,d], A. Laref [a,*], S. Alterary [b,c], S. Faraji [d], M. Alsalhi [a]

[a] Physics Department, Faculty of Science, King Saud University, Riyadh, Saudi Arabia
[b] Chemistry Department, Faculty of Science, King Saud University, Riyadh, Saudi Arabia
[c] King Abdullah Institute of Nanotechnology, King Saud University, Riyadh, Saudi Arabia
[d] Zernike Institute for Advanced Materials, University of Groningen, the Netherlands

ARTICLE INFO

Article history:
Received 18 March 2021
Accepted 20 June 2021
Available online 25 June 2021

Keywords:
2D layered materials
MoS_2
PLD
Structural morphology
Electronic structure
Point native defects
Optical properties
Energy storage
Next generation 2D-material devices

ABSTRACT

The two-dimensional (2D) layered molybdenum disulfide (MoS_2) material represents a nominee potent for optoelectronic devices application. In this research work, the experimental characterizations of 2D- MoS_2 thin films are reported in terms of various microscopic and spectroscopic techniques. The synthesized MoS_2 thin films are grown by employing the pulsed laser deposition (PLD) procedure on SiO_2/Si substrates. In order to monitor the deposition rates of ablated films, the buffer argon-gas pressures are varied during the pulsed laser deposition at substrate temperature of 700 °C. The field emission scanning electron microscopy and atomic force microscopy analyzes revealed a change in the surface morphology of MoS_2 films when the buffer Ar-gas pressure is varied between 0 and 100 mTorr. For all samples, a 2H-phase is revealed from X-ray diffraction patterns, indicating a reflection (2θ) around 14.85°. By varying the deposition pressure of laser-ablated MoS_2 films, the X-ray photoelectron spectroscopy divulged the chemical compositional elements and valence states of Mo and S on the surface of MS_2 films with low density of defects. Analysis of the photoluminescence spectroscopy illustrated emission bands spanning from the visible (Vis) to near-infrared (NIR) regimes in the deposition pressures range ~ 0–100 mTorr. This is mainly owing to the change in the recombination of electron–hole pairs and charge transfer between the deposited MoS_2 films and SiO_2 substrate surface under various buffer gas pressures. Additionally, first-principles electronic structure calculations are performed to qualitatively examine the effect of native point-defect species (sulfur-monovacancy and sulfur-divacancy defects) on the electronic structure and optical properties of 2D- MoS_2 sheets. It is unveiled that the variation of compositional sulfur-vacancy defect in MoS_2 monolayer creates an in–gap defect levels above the valence states, leading to an acceptor character. Importantly, the enhancement in the optical absorption spectra divulged a shift in the optical gap from Vis-NIR window with the increase of sulfur vacancy contents in MoS_2 single-layer. The identification of intrinsic point defects may be beneficial for photovoltaic energy conversion at higher wavelengths by designing next generation 2D-semiconductors,

* Corresponding author.
E-mail address: amel_la06@yahoo.fr (A. Laref).
https://doi.org/10.1016/j.jmrt.2021.06.059

which could be of vital significance for growing 2D layers and multilayers into practical technologies.

1. Introduction

New plethora of two dimensional (2D) layers has captivated a worthwhile enthusiasm owing to their distinctive characteristics [1–3]. Recent evolution in the layered 2D materials has comprised enormous benefits for devices fabrication, such as dielectric, semiconductor, and conductor layers [4–8]. The synthesized 2D layered materials have acquired an outstanding performance for the new generation 2D-devices, like photodetectors, flexible thin film transistors, phototransistors, heterogeneous catalysis, heterojunction diodes, gas sensors, and lithium ion batteries [9–14]. Transition metal dichalcogenides (TMDs) are classified into the category of the most promising 2D layered materials. The atomically thin molybdenum disulfide (MoS_2) belongs to 2D-TMD materials, containing layers weakly interacting and could be isolated from its bulk parent compound. Accordingly, the 2D-MoS_2 layered atomic structure possesses distinctive and flexible optical transparency. This is owing to the tailoring of its indirect band gap of 1.2 eV of bulk semiconductor to the direct transition via the thinning to a few layers number unlike the semi-metallic behavior of graphene [15–21]. By thinning bottomward to monolayer, MoS_2 exhibits striking electronic, optical, and mechanical characteristics. However, Van der Waals interactions constitute the bonding of inter-layered S–Mo–S via the strong covalent bonding between Mo and S atoms in the basal plane. Both experimental and theoretical realizations revealed a wide direct band gap ~1.9 eV for the single layered MoS_2 material and exhibited a significant photoluminescence as well as superior quantum efficiency [19–22]. Furthermore, single-layer and few-layered MoS_2 material induced peculiar electrical and optical performance, significant carrier mobilities between 200 and 500 cm^2/V, and outstanding ratios of on/off current exceeding 10^3. This can turn this promising 2D material accessible into the field-effect transistors (FETs) application and the thinnest transistor based on MoS_2 was previously proposed [23–26]. Eventually, MoS_2 is regarded as an eminent candidate for the next-generation electronic devices because of its extraordinary valley, excitons, and spin behaviors [27–30].

Up to date, various researches have been focused on the preparation of MoS_2 layers by utilizing diverse experimental techniques, the so-called lithium intercalation, magnetron sputtering, liquid exfoliation, mechanical exfoliation, chemical bath deposition, laser thinning, and chemical vapor deposition (CVD) [31–37]. The disadvantages of the chemical synthesis and mechanical exfoliation techniques are related to the inconvenience of handling large area for practical devices [34–36]. Despite the simplicity, the scalability, and short time consumption of the magnetron sputtering, the shortages are attributed to the roughness of crystal, poorness quality of crystal, and the consumption of elevated energy [37–40]. By employing CVD procedure, the nucleation of layer is troublesome, which induces non-uniformed MoS_2 layers. Also, it is possible to manipulate the thickness and scale size of samples. The growth time is lengthy that can only be facilitated at higher temperatures. However, it is necessary to look for an alternative procedure with several advantages over the traditional growth methods, like pulsed laser deposition (PLD). This is due to its simplicity, safety, cleanness, accessibly controllable, low price, rapidity, scalability, highly manipulation, and lower contamination during the growth process. The preparation of layered MoS_2 films by using the PLD technique provides various benefits comparatively to the traditional CVD procedure, where the stoichiometric transmission of ablated species can be established from the target into the substrate. The monitoring of thickness would be attained by controlling the growth kinetics and repetitive rate (frequency) under the change of deposition pressure and laser energy. Thus, the PLD procedure is proper for the growth of multi-elemental elements at different stoichiometry parameters in order to prevent the use of costly and likely risky precursors (i.e. H_2S) utilized in other synthesis techniques [41–46]. Heretofore, the PLD technique has been effectively employed in the deposition of various 2D-layered materials, like graphene, black phosphorous (BP), MoS_2, and WS_2, and so on [46–48]. This technique is a useful step for a large scale deposition of multi-elemental layered materials fabricated in a wafer-scale of electronic devices.

It is well recognized that the intrinsic point defects in 2D materials can significantly alter their chemical and physical properties, yielding either wanted or undesirable response. The previous works have been already focused their attention on the vacancies defects that affect the change of magnetic levels in graphene and boron nitride [49–51]. From the experimental perspectives, the mono-sulfur vacancies remain the most prevailing defects, divulging both acceptor and donor behaviors [52–56]. It was reported that the insertion of oxygen vacancies is much accessible than the rest of native point defect species. Thereby, the impurity states will be created in both valence states and in band gap level. Subsequently, the impurity levels resulting from the low composition of native point defects, may enhance the photon absorption in the visible light regime useful in photovoltaic energy conversion at higher wavelengths. Extra native point defects of constituent atoms, the so-called anti-sites, vacancies, and interstitials of the host atoms would contribute to the reduction in the bond strain by incorporating the doping impurity with different atomic sizes. Thereby, the charge imbalanced can be compensated via the aliovalent impurity atom and the electronic structure of semiconducting material would be altered nearby Fermi level. In contrast to the oxide analogous materials, the annealing process is troublesome in

a gaseous environment with sulfur atoms. Thermodynamically, MoS_2 materials containing sulfur are not easy to be stabilized comparatively to oxide analogous materials. Various stable or meta-stable allotropic materials based on sulfur may constitute hypervalent molecules, although, the stabilization of MoS_2 samples without native defects is more difficult than the oxide materials. However, the stabilized oxide materials are much easier for the manipulation of partial pressure of O_2 by employing the annealing process at higher temperature.

For this key purpose, we address experimental investigations on the structural and optical characteristics of MoS_2 thin films deposited on SiO_2/Si substrates by employing various characterization instruments under the influence of buffer Ar-gas pressures in the range of 0–100 mTorr. The depositions of laser-ablated MoS_2 thin films on SiO_2/Si substrates, are carried out using PLD technique. In order to control the structural morphology of the samples, the deposition of thin films are cautiously prepared from the MoS_2 targets grown on SiO_2/Si substrates by varying the buffer Ar-gas pressure and selecting a proper ablated laser pulse number at substrate temperature of 700 °C. The morphology of surface, thickness size, and optical features of MoS_2 films are found to vary versus the change of deposition pressure rate. By employing the PLD technique, it is possible to minimize the typical vacancies in the prepared specimens. It was found previously that the S vacancies contribute into the degraded electronic and optical characteristics of the 2D-materials [54–56]. Hitherto, the decisive relationship between the vacancy defects and the degraded physical features of MoS_2 layered atomic structures was a disclosed inquiry. The most dominant defects in MoS_2 layered structures are instances of lacking mono-S atoms, which are created from S-mono-vacancies. All the above mentioned potential issues, triggered our attention to report first-principle calculations to examine the impact of intrinsic defects, like mono-sulfur vacancy (V-S), di-sulfur vacancy (V-S_2) on the physical properties of MoS_2 monolayers that are supportive to our experimental investigations. The creation of both V-S, and V-S_2 typical native defects in the host lattice can tailor or enhance the electronic and optical behaviors of MoS_2 single-layer, to find desirable properties, which are missing in the pristine monolayers [57–68]. A deep acceptor-like state would be created in the host material with the presence of native point defect, leading to a p-type semiconductor. The intrinsic defects describe a proper route for the next generation 2D-semiconductor devices which could be indispensable for growing 2D layers into realistic industrialized technologies.

2. Materials and methods

2.1. Experimental setup

In the PLD setup, a plasma plume is generated by ejecting the energy laser pulse of MoS_2 specifies on the substrate that is placed at a few cm in front of the target. In order to control the morphology and deposition rate of structural materials, various parameters are needed to be monitored suitably, such as the excitation voltage, laser energy, number of ablated laser pulses, repeating rates, and pressure of background gas. The growth mechanisms are optimized and performed on SiO_2/Si substrates by setting a laser pulse of 20,000 on the MoS_2 target to eject a similar quantity of material at each deposition step. For SiO_2/Si substrate, the growth temperature of 700 °C is selected for the deposited samples. The generated plasma that involves both ions and atoms, will attain the substrate at striked laser pulses on the solid target of MoS_2. Then, Mo and S atoms are implanted onto SiO_2 substrate surface at a reduced time, which is undertaken as the source of atoms during the delivering of an energetic source of PLD. Moreover, the SiO_2 surface acts as a growth template for MoS_2 films. A cautious manipulation of MoS_2 particles number is carried out on the SiO_2 surface of the resulting films. This procedure can be established by changing the laser energy and time of deposition. The films quality can also be organized by selecting suitable rates of cooling and pressures of background gas. The deposited MoS_2 films are carried out on cleaned and polished SiO_2 substrates.

The deposition of MoS_2 films is achieved by employing a KrF laser ($\lambda = 248$ nm) Lambda physik excimer PLD system. The distance between the target and substrate is selected at 5 cm. Before the deposition of samples, the chamber is evacuated at a base pressure of $<10^{-7}$ Torr for preventing the oxidation of MoS_2 films. The ablated MoS_2 target is implemented on SiO_2/Si substrate at an excitation voltage of 22 Kvolt, a frequency of 10 Hz, and a duration of pulse of 20 ns. The time of ablated target is realized at 10 s to prevent the transfer of MoS_2 species (less than 5 nm) onto the substrate. The laser spot size is focused on the target at 1 mm^2 by utilizing the ablated laser of fluence ~6 J/cm^2, which possesses a circular outline of a radius ~7 cm. Then, the sample was delivered inside the chamber of preparation (buffer Ar-gas pressure ~ 0 mTorr) after the PLD procedure. For the deposited samples, the cooling of SiO_2 substrate surfaces are established at rates of 3 °C/min. The samples are synthesized at various buffer Argon gas pressures of 0, 50, and 100 mTorr, respectively. A commercial pellet of MoS_2 (Stanford advanced materials) is utilized as a sputtering target with purity of 99.9%. The PLD-grown MoS_2 films are implemented at a dimension of 10 mm × 10 mm on a cleaned surface of SiO_2/p + -Si wafer substrates of 50 nm thickness. The fabricated MoS_2 films on SiO_2/Si substrates illustrated a particle-like structure because of the sensitivity of SiO_2 surface [40–43]. Fig. 1 displays the experimental setup of PLD system that is employed during the growth of MoS_2 films. To improve the quality of films, a suitable choice of laser fluence and cooling rate are required. For the preparation of various samples, a flowing of buffer Ar gas (pressures of 0, 50, and 100 mTorr, respectively) and a diffusion pump are used for both target and substrate that are settled inside a vacuum chamber. In order to acquire less S deficiency during the deposition process, the buffer Ar-gas is utilized for the control of pressure in the chamber and stoichiometry of deposited films.

2.2. Thin film characterization and measurements

After the PLD synthesis of MoS_2 films, the morphological shapes of structures (the variation of magnitude is between nm and μm) are measured and characterized by changing the

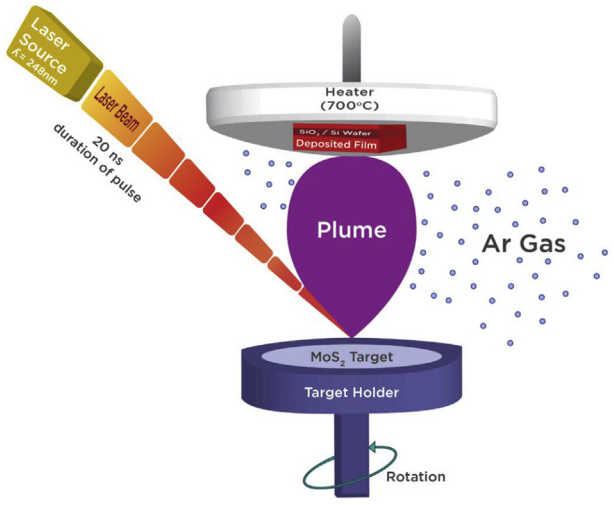

Fig. 1 – Schematic diagram of deposition of MoS_2 films by PLD technique.

buffer-Ar gas pressure from 0 mTorr up to 100 mTorr. The structural characterizations of MoS_2 samples are carried out with X-ray diffractometer (XRD) patterns, a Philips PW1710 diffractometer, while the radiation source of Cu-Kα is used with a wavelength of 0.1542 nm. The structural morphologies are analyzed by employing the field emission scanning electron microscopy (FE-SEM; JSM-7610 F FE-SEM; JEOL) of MoS_2 films that are grown on SiO_2/Si substrates. In addition, the surface topography of MoS_2 films are determined from the atomic force microscopy (AFM; Bruker, Germany). The changes in the structural bonds and transmission modes of MoS_2 samples are estimated by means of Fourier transform infrared (FTIR; Nicolet 6700, Thermo Scientific, USA) spectra as a function of the variation of wavenumbers between 350 cm^{-1} and 4000 cm^{-1}. Additionally, the measurements of optical absorbance spectra of MoS_2 films are determined via the ultraviolet–visible–near infrared (UV–Vis–NIR) spectroscopy (JASCO UV/VIS/NIR spectrophotometer (V670)) by varying the wavelengths between 200 nm and 1200 nm. The binding energies of Mo, and S elements in MoS_2 films are measured from the monochromatic Al Kα at 1486.6 eV, with X-ray photon spectroscopy (XPS) (PHI 5600 Multi-Technique XPS: Physical Electronics, Lake Drive East, Chanhassen, MN, USA). The photoluminescence (PL) spectroscopy is utilized for the measurements of emission spectra of all samples at continuous wave laser of 473 nm.

3. Results and discussion

The effect of deposition pressure on the crystalline patterns, chemical stoichiometry, and optical characteristics of the layered MoS_2 films are discussed in this section. The variation of deposition pressure influences MoS_2 thickness on the substrate surface by selecting proper PLD deposition parameters.

3.1. Structural characterizations

3.1.1. FE-SEM analysis

The FE-SEM measurement is a useful tool to inspect the changes in the morphological, surface characteristics, and structural properties of the specimens grown at different deposition pressure regimes. Fig. 2(a)–(c) illustrate the high resolution SEM images of the deposited MoS_2 films on SiO_2/Si substrate surfaces. After PLD procedure, the Mo and S species can be grown conveniently on the substrate surfaces during the deposition process and substrate cooling. Therefore, the deposition pressure is crucial to alter the mean free path of the ablated species in which the energy will be maximized or minimized to arrive the substrate surface. The nucleation of MoS_2 nanostructures occurs at the first stage on the substrate after the deposition process at different buffer Ar-gas pressures (see Fig. 2(a)–(c)). This may be associated with the different domain boundaries formed of agglomerated structures having different orientations. The FE-SEM images reveal twisted triangular domains for the synthesized MoS_2 films under the variation of buffer Ar-gas pressures, as portrayed in Fig. 2(a)–(c). After optimizing the growth conditions, the layered MoS_2 nanostructures acquired polycrystalline patterns with hexagonal shape. The formation change of triangular islands is associated with the growth environment of MoS_2 films at deposition pressures of 0, 50, and 100 mTorr, respectively. Obviously, the modification of nanoparticles arrangement induces in laser ablated MoS_2 films under the variation of buffer Ar-gas pressures. The SEM image displays that the prepared MoS_2 film from target possesses layered structures at deposition pressure of 0 mTorr, while various zones contain wavy-type structures (see Fig. 2(a)). The nucleation and Van der Waal layers occur on substrate from MoS_2 nanostructured films that have flakes arrangement along different directions. As pictured in Fig. 2(b), small nanocrystals are grown on SiO_2/Si substrate surface. Therefore, the deposited film illustrates shapes of gradual triangular islands when the deposition pressure is increased up to 100 mTorr (see Fig. 2(c)). The coverage of MoS_2 is almost complete on the substrate surface at 100 mTorr, as anticipated to grow layer-by-layer mode. Thus, the structural morphology of MoS_2 films on the surface of SiO_2 substrate, confirms pyramidal patterns. In PLD processes, only the stoichiometry is transferred from the target onto the substrate and the crystalline phase of the resulting film is not necessarily similar to the target. At 0 mTorr, the appearance of resputtering from the film surface is owing to the existence of energetic particles inside the plasma plume. Conversely, a reduction in the particle energy is accompanied with a reduced resputtering as the gas pressure augments. Then, the scattering of ablated Mo and S atomic species getting out of the deposited path between the target and substrate surface will be increased at 100 mTor. This may conduct to a reduction in the deposition rate. At higher deposition pressure, the kinetic energy would be diminished for the deposited particles to attain the optimal deposition rate and to prevent the particles implantation. Thereupon, the deposition of the films from the target would

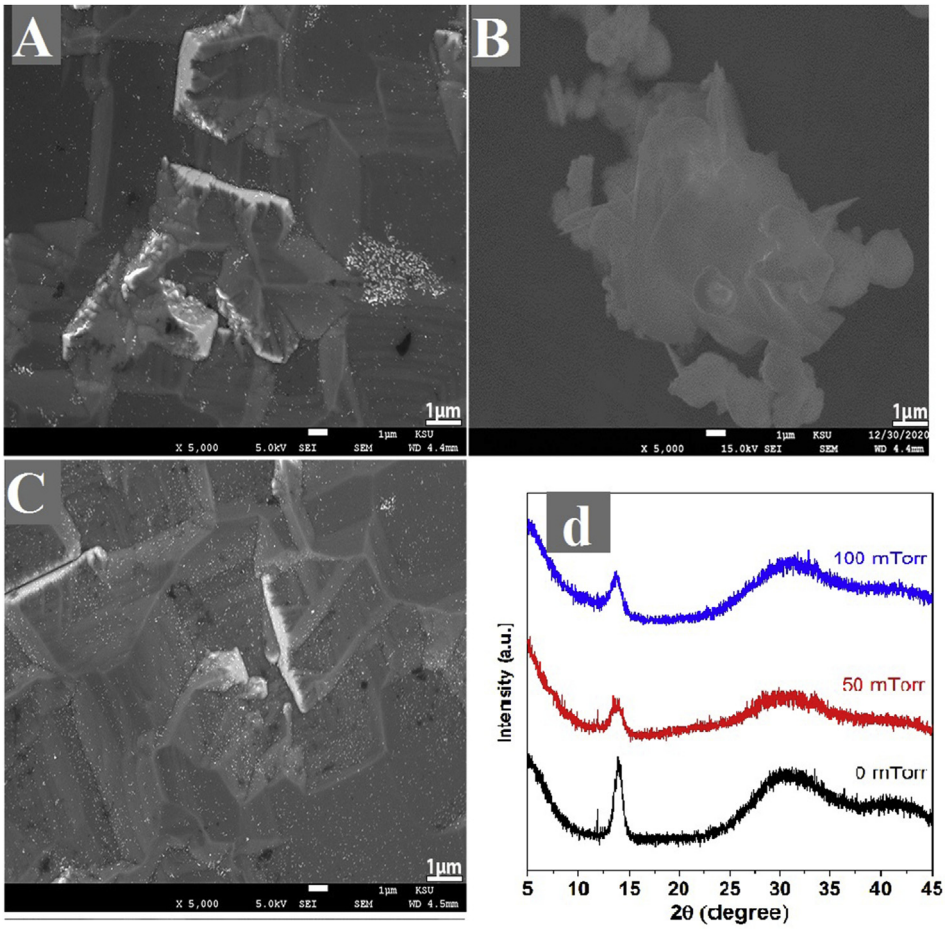

Fig. 2 – (a) FE-SEM images of MoS_2 films deposited on SiO_2/Si substrate prepared at 0 mTorr, (b) 50 mTorr, (c) 100 mTorr and d) X-ray diffraction patterns of all samples deposited at 20,000 pulses on SiO_2/Si substrate.

be grown at various stoichiometries. At deposition pressures of 0 mTorr, 50 mTorr, and 100 mTorr, the Mo/S ratios are 0.75, 0.54, and 0.54, respectively. The variations between the three samples, are subject to the minor local stoichiometry alterations in the films, owing to the depleted areas from sulfur. At elevated deposition pressure, the loss of sulfur element is reduced during the laser ablation against the deposition process in the vacuum.

3.1.2. *XRD characterization*

The crystalline structure and layer spacing of laser-ablated MoS_2 films are assessed by using XRD measurements. For a suitable control of the structural morphology of samples, the buffer Ar-gas pressures are varied between 0, 50, and 100 mTorr, respectively. Accordingly, the XRD patterns of the three prepared MoS_2 films are portrayed in Fig. 2(d), which are recorded in 2θ range of 0–45°. They exhibit broad and sharp diffracted peaks. Then, the synthesized MoS_2 films are ascertained from the intensity of diffracted peaks taking place between 14° and 36°. Apparently, the three samples display quite similar XRD patterns with some details at 2θ varying between 13.5° and 36°. In Fig. 2(d), the pronounced sharp peaks that occurred in the three samples, illustrate observable reflections at 2θ = 14.85°, 15.02°, and 15.16°, in the deposition pressure range of 0, 50, and 100 mTorr, respectively. These characteristic peaks are assigned to (002) crystallographic plane of hexagonal (2H– MoS_2) phase, appertaining to the P63/mmc space and describing the well-recognized standard spectrum (JCPDS 00-37-1492) [45]. For all samples, the feature peak (002) is indicated by the in-plane along C-direction of MoS_2 material, proposing layered structures with interlayer spacing of 0.625 nm. The structural formation permits the crystallization of the deposited particles of MoS_2 film at 0 mTorr because of the first peak sharpness. The second superimposed broadened peaks emerge around 34.3°, 35.3°, and 35.7°, respectively, corresponding to (101) plane. They are due to the partial restacking of few layers along the deposition procedure. Also, the intensity of first peak is decreased when the deposition pressure of buffer Ar-gas is increased. The second peak position of MoS_2 film is relocated somehow to a higher position due to the variation of sulfur deficiency in the MoS_2 flakes. Thus, the discernible peaks are related to the hexagonal crystalline phase of MoS_2 films and other polycrystalline phases with the existence of some impurity phases of SiS_2 and MoO_3, which are induced from the interaction between the films and substrate surfaces under the variation of deposition pressure.

From X-ray diffraction based on Scherer equation, the thicknesses of MoS_2 films, are found around 17.3, 15.7, and

14.1 nm, respectively for the three samples (buffer Ar-gas pressures ~ 0, 50, 100 mTorr, respectively). The decreased intensity of the feature peak (002) reveals the stacked MoS_2 layered films along the C-axis, which is due to the reduced of thickness size at higher deposition pressures. This may reflect the nanocrystalline behavior of MoS_2 films. It can be attributed to the dissipation of kinetic energy out of the ablated species that are scattered in the presence of gas Ar atoms. Furthermore, the ablated particles will scatter significantly as the deposition pressure increases, and the particles number will be reduced to arrive onto the substrate surface. Then, the surface mobility of the species diminishes after arriving to the substrate at higher deposition pressure because of their reduced kinetic energy. As inspected from the morphology of synthesized MoS_2 films, the particle size decreases as the deposition pressure increases. Thus, the diffraction patterns indicated the mixture of trigonal structure with insignificant intermediate phases of SiS_2 and MoO_3 [44–46]. At various buffer argon-gas pressures, the deposited MoS_2 films have polycrystalline behavior with a hexagonal crystallinity shape and their physical properties are analogous to MoS_2 flakes comprising S-vacancy type defects.

3.1.3. *AFM characterization*

To acquire an insight on the surface homogeneity and structural morphology of the grown-PLD MoS_2 samples at different conditions, the high resolution AFM images are inspected. Fig. 3(a) and (c) depict the AFM topographies of MoS_2 structures deposited on SiO_2/Si substrate surface at various buffer gas pressures. At 0 mTorr, the MoS_2 film has a polycrystalline distribution on the entire surface, constituting few isolated aggregates on the top of substrate. However, the favorable formation of MoS_2 film is composed of layered nanoclusters with brighter aggregated structures that are partially embedded on the top of SiO_2 surface, as seen in Figs. 3(a)–(c). It is noticeable that the deposited MoS_2 sample at 0 mTorr, starts its growing with the nucleation of atomic islands. Subsequently, the Mo and S atomic species are favorably occupied atop substrate surface, and their micrographs are illustrated by bright spots with images of atomic resolutions. The inspection of AFM topography of MoS_2 film characterized at 50 mTorr, exhibits the growth of triangular shapes comprising few layered MoS_2 with wider lateral sizes. Consequently, this sample encompasses flake pattern of few-layered MoS_2 films. The surface of MoS_2 nanocrystals illustrates also irregular morphological patterns because of the existing of various defective points, as portrayed in the AFM images of Fig. 3(c). For the formation of crystalline films with Van der Waals layers, the interaction of MoS_2 layers occurs on the underlying substrate. At deposition pressure of 100 mTorr, the atomic nucleation of MoS_2 island patterns, is indicated by atomic resolution images with brightest spots due to the sulfur deficiencies on the substrate surface. The notches under the brightest spots reflect the nearest neighboring of Mo elements with S atoms in trigonal configurations, which contain few-layered MoS_2 triangular islands. When the deposition pressure increases, the substrate surface will be covered with Mo and S atomic species as flat grains with diminished size of aggregates and the particles assemble in disk shaped islands. AFM images of the synthesized films under various deposition pressures, exhibit a reduction in the RMS surface roughness as the deposition pressure increases. At 0, 50, and 100 mTorr, the averaged roughness values are around 12.5 nm, 4.5 nm, and 1.75 nm, respectively. Thus, the systematic reduction in the RMS surface roughness and crystallites size are detected with the increase of buffer Ar-gas pressure. This can be attributed to the decrease in the kinetic energy when the ablated Mo and S particles are scattered out of the path of deposition by the gas Ar atoms. Also, the deposition rate reduces due to the scattering of ablated species with Ar-gas atoms and the aggregates size diminishes comparatively to the deposited samples at 0 mTorr. Thereupon, the MoS_2 species that are ablated from the target possess an elevated kinetic energy to arrive quickly to the substrate. The increase in the deposition pressure leads to the increase in the collision of ablated atomic species with Ar molecules inside the chamber. Therefore, the film fabricated at 100 mTorr, characterizes the thinnest MoS_2 islands and comprises the smaller triangular pattern of few-layer MoS_2. Interestingly, the MoS_2 thickness size is marginal irrespective to the recognized distance of interlayer in the MoS_2 bulk structure (6.15 Å [54–57]). Eventually, the deposition pressure variation is a good signature for the alteration of the growth process of samples, although the aggregates size of MoS_2 nanocrystals have been modified at elevated deposition pressure.

3.2. *XPS characterization*

The XPS measurements are moreover utilized to inspect the films evolutions and to ascertain sulfur deficiencies in MoS_2 films under the variation of buffer Ar-gas pressures. From the XPS spectrum, the compositional elements and bonding

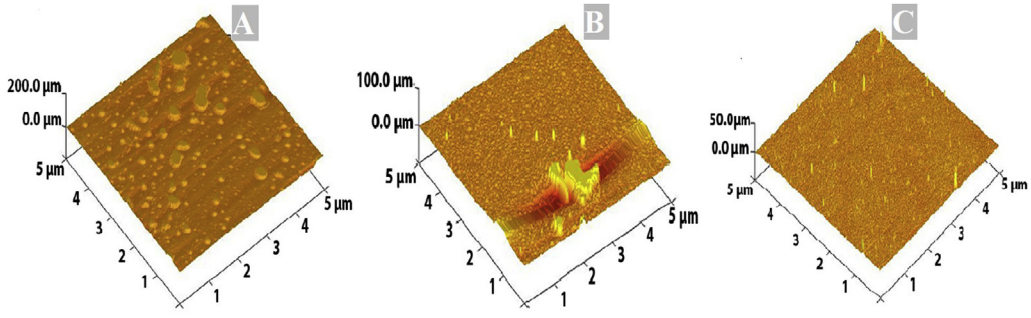

Fig. 3 – AFM of MoS_2 nanostructured films achieved on SiO_2 wafers at 20,000 pulses (a) 0 mTorr, (b) 50 mTorr, and (c) 100 mTorr, respectively.

character in MoS_2 films are identified. A survey scan of the high-resolution profile corresponding to these compositional elements is displayed in Fig. 4. These compositional elements, such as Mo, and S occur at some distinct regions of XPS survey spectrum. As apparent, the characteristic peaks analysis of S 2p, and Mo 3 d core levels, respectively, appear at certain binding energies (Fig. 4). The plot of Mo 3 d core level illustrates an intense sharp peak around 230 eV which is diminished and relocated to lower binding energies at 228, and 225 eV at deposited pressures of 50 mTorr and 100 mTorr, respectively. At 0 mTorr, a weak peak sited at 169 eV, is attributed to S 2p profile, although two feature peaks reduce that are split into doublet $Sp_{1/2}$ and $Sp_{3/2}$ and shift to lower binding energies around 165 and 166 eV, for deposition pressures of 50 mTorr and 100 mTorr, respectively.

For all samples, the schematic XPS spectra of Mo 3 d core levels measured in different deposition pressures (0, 50, and 100 mTorr), are depicted in Fig. 5. The characteristic peaks of Mo 3d states reveal the essential binding energies for the deposited MoS_2 thin films from the targets as a function of the change of buffer Ar-gas pressures. As apparent from Fig. 5 (a)–(c), four typical peaks of Mo 3 d states are determined, and their corresponding values are gathered in Table 1. Two characteristics peaks corresponding to the $Mo3d_{5/2}$ and Mo $3d_{3/2}$ concomitant states, respectively, are assigned to the Mo^{4+} state in MoS_2 films (see Table 1). Two core level peaks associated to the Mo^{6+} $3d_{3/2}$ and Mo^{6+} $3d_{5/2}$ species, emerge from the oxidation of Mo atoms in the films. It is likely that the implantation of Mo atoms occurred on SiO_2 substrate surface. Also, the reaction may be stemmed with oxygen when the sample is taken out of the chamber, leading to an intermediate phase of MoO_3. From the XPS spectra of the deposited films at higher buffer Ar-gas pressure, the amplitude of peaks reduces compared to the film prepared at 0 mTorr. However, the laser-ablated MoS_2 films affirmed smaller peaks of S atom due to the lower S vacancies at both 50 and 100 mTorr, respectively. A disorder is generated around the surrounding atom because of the lower S defects, which is subject of lower peaks intensity of Mo3d, and S 2s atoms in the film compared to the synthesized films at 0 mTorr. Low intensities are developed in the spectral peaks at higher deposition pressures, which are assigned to the S 2s state and S vacancies in MoS_2 films. Also, the relocation of Mo^{4+} 3 d doublet takes place at the lower binding energy ~0.1 eV, which suggests a low degree of sulfurization of Mo at higher deposition pressure. Then, the increased deposition pressure yields a reduction in the Mo 3 d spectral peaks. Thereby, the feature Mo peaks are narrower for the films deposited in the vacuum chamber, containing more sulfur defects. For the three samples deposited from the target at various pressures, the change in the S2p core level regimes is detected for the film obtained at 0 mTorr, as portrayed in Fig. 5 (a)–(c). During the ablation procedure, the evaporation of sulfur atoms arises from the target which enables the change in the stoichiometric MoS_2 prepared on the substrate at low and high deposition pressures.

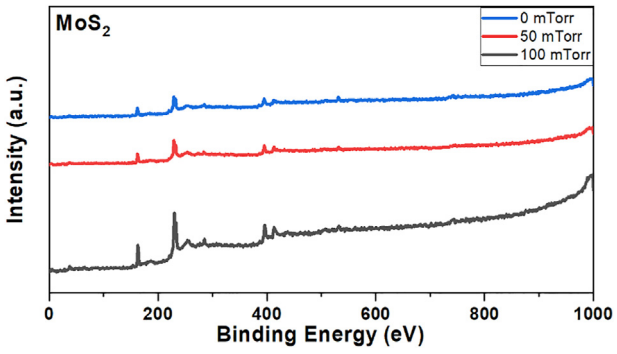

Fig. 4 – XPS survey spectra of MoS_2 films fabricated using different deposition pressures at 20,000 pulses.

The dissimilarities in the XPS spectra acquired in the three samples can be elucidated by changing the deposition pressures (see Fig. 6). The ejection of Mo and S atoms took place at a specific energy amount after the laser ablating the target. The samples are eventually cooled down at 3 °C/min, although, the temperature of 700 °C was fixed directly after the interruption of ablated laser nearby the equilibrium conditions. Sufficient heat was hence kept in such a way the Mo and S atoms acquired enough mobility for reorganizing themselves and thereby a quite ordered crystalline structure can be achieved. Hence, the deposition of Mo and S atoms implanted onto SiO_2 substrate surface, took place in the vicinity-surface areas of the film. However, the formation of SiS_2 at the surface areas of the film emerges from the interaction of S atoms on the substrate surface [44–46]. The reaction of the rest of S atoms occurs on the sample surface with Mo atoms to acquire the formation of MoS_2 on top of the SiO_2 layer. In the S 2p spectra, the doublet $Sp_{1/2}$ and $Sp_{3/2}$ peaks of MoS_2 films fabricated at various pressures are collected in Table 2. This is due majorly to the Fermi level pinning that originates from sulfur vacancies. The defective structures acquire a displacement to the lower binding energies of the Mo^{4+} 3 d peaks via the XPS spectra. At 0 mTorr, the excessive Mo species are developed in MoS_2 films grown on SiO_2, substrate surface right after the formation of MoS_2 films comparatively to the two samples prepared at higher deposition pressures. This can be referred to the extra S atoms that are consumed in the formation of SiS_2. However, the excessive Mo atoms are preserved as metallic in the vacuum. Their reaction with oxygen emerged upon the exposure to the atmospheric conditions to achieve the oxides, which may sit on top of the MoS_2 layer, as inferred via the XPS characterizations. Control of the chemical composition and crystallinity of the synthesized MoS_2 films can be established by varying the buffer gas pressure. Then, the argon gas pressure affects chiefly the acceleration of sulfur deposition rate without notably accelerating the Mo deposition rate. This can be reflected to the pulsed laser procedure, while the voltage excitation will also enable the formation of a quite ordered structure comprising Mo and S atoms at a short time of cooling.

3.3. *FT-IR characterization*

The elements bonding comprising the attachment of functional with different vibrational modes groups, are assessed by using the IR spectrum. For the sake of comparison, the spectra are represented at various deposition pressures for the synthesized MoS_2 samples, as depicted in Fig. 7. The FTIR

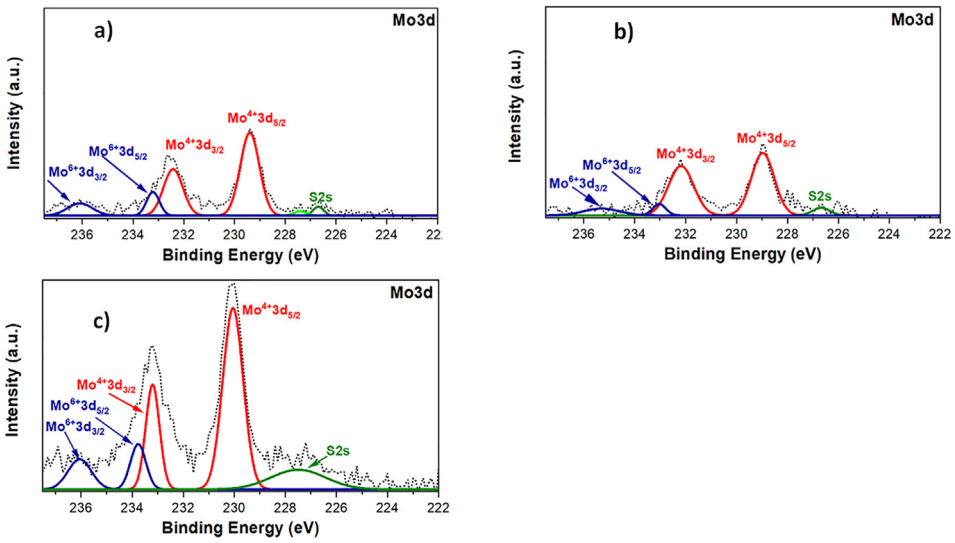

Fig. 5 – XPS spectra of Mo3d core level for MoS_2 films prepared at 20,000 pulses: (a) 100 mTorr (b) 50 mTorr. (c) 0 mTorr, respectively.

profiles of the PLD grown MoS_2 films on SiO_2/Si substrates reveal the change in the peak position and intensity of vibrational modes which report the modification in the stretching and bending vibrational modes undergoing between the lower and higher frequency regimes. The FTIR inspection of MoS_2 films displays specific vibration modes, resulting from the alteration of Mo–S bonds under various deposition pressures. The vibrational modes of MoS_2 groups and some other elements arise from the Si–S and Mo–O interactions between films and substrates. The low transmitted peak occurring around ~1098 cm^{-1}, alluded to the S–O stretching bonds, although the broad IR peak at around ~3450 cm^{-1} is attributed to the Mo–O bonding after the interaction of films with the substrate surfaces. Also, the FTIR spectrum illustrates a sharp peak located around ~2300 cm^{-1}, owing to the stretching and bending of O–Mo vibrations. Marked peaks positioned at 450 cm^{-1} are credited to the S–Mo–S bond stretching of the Mo–S bonds which reduce with the increase of deposition pressure as well as the Si–O stretching bond, respectively. Moreover, these characteristic peaks emerge from the Mo–S bonding in MoS_2 films. The IR plots of MoS_2 films prepared at various deposition pressures, contain two lower and elevated vibrational characteristic modes, which display an insignificant shift in the expected vibrational modes of MoS_2 spectra. With the change of deposition pressures, the dissimilarities in the vibrational modes are owing to the dipolar interaction between the SiO_2 substrate and MoS_2 films. This behavior was mainly related to the change in the interaction between the substrate and sulfur atoms, as well as the electrostatic surroundings that influence the MoS_2 vibration modes [33,36,43,45]. According to the AFM measurements, it is noticeable that the films are quite thin, corroborating the vibrational modes of FTIR of MoS_2 films. The intensity variation in these IR peaks can be a good indication of S defects in the thin films fabricated at various deposition pressures. As apparent form FTIR spectra, the S-vacancy is a favored position for the interaction of Van der Waals interlayer without a significant bond creation via the S-vacancy.

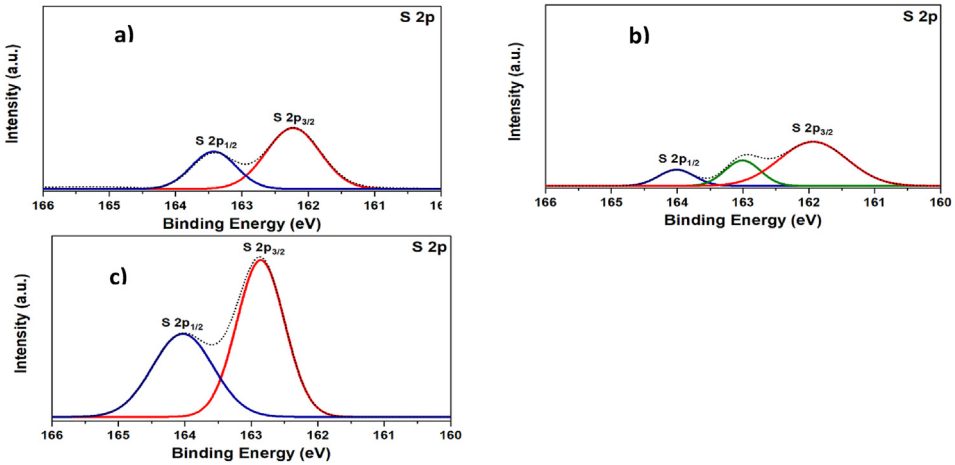

Fig. 6 – XPS spectra of S 2p core level for MoS_2 films prepared at 20,000 pulses: (a) 100 mTorr (b) 50 mTorr. (c) 0 mTorr.

Table 1 – The binding energy peaks of Mo and S states extracted from Mo3d core level for MoS_2 films at 100 mTorr, 50 mTorr, and 0 mTorr, respectively.

peak	Binding energy (eV) 100 mTorr (a)	Binding energy (eV) 50 mTorr (b)	Binding energy (eV) 0 mTor (c)
Mo^{6+} 3d $_{3/2}$	236	236.1	235.3
Mo^{6+} 3d $_{5/2}$	233.8	233.2	233
Mo^{4+} 3d $_{3/2}$	233.2	232.5	232.2
Mo^{4+} 3d $_{5/2}$	230	229.4	229
S2s	227.4	226.7	226.6

These results support the XPS spectra finding, which indicate the effective interaction between the compositional elements of MoS_2 films and substrate surface under various deposition pressures.

3.4. *Optical properties*

3.4.1. *Photoluminescence measurement*

Analysis of the electronic and optical properties of MoS_2 films, can be revealed within PL spectroscopy. A wavelength of 473 nm (~2.64 eV) of excitation source was selected by pumping the light in MoS_2 films. The PL emission profiles are registered for the three synthesized samples at 0, 50, and 100 mTorr, respectively, that can divulge both excitonic-emission bands in the Vis-NIR spectrum (see Fig. 8(a)). From the PL plots, the laser-ablated MoS_2 films possess a direct band gap at different deposition pressures, as displayed by the PL emission signal around 1.65 eV that is associated with the recombination of excitons. Thus, the band gap results in electron–hole pairs with transition spanning from the Vis-NIR window, corresponding to the red light. For the deposited samples at 0, 50, and 100 nm, the emission bands reveal feature peaks sited at wavelengths about 759, 760, and 761 nm, respectively, indicating a direct excitonic transitions of the K point in the Brillouin zone [3,20–22]. The relaxed excitons of MoS_2 films will induce in the photons emission of an energy band gap ~1.9 eV at the K-point. Hence, the PL analysis enables us to detect the quantum confinement in MoS_2, which is correlated to the band gap as well as the energy transitions correspondence with the interlayer interaction in MoS_2. The alterations in the band gap is insignificant when the deposition pressure is increased in the samples, which indicates that the semiconductor features are broadly restored via the photoluminescence. The PL spectra illustrate a broad peak with marginal amplitude occurred at elevated energies, owing to the substrate effect. Pronounced PL emission signals revealed

Table 2 – The binding energy peaks of S states extracted from S 2p core level for MoS_2 films at 100 mTorr, 50 mTorr, and 0 mTorr, respectively.

peak	Binding energy (eV) 100 mTorr	Binding energy (eV) 50 mTorr	Binding energy (eV) 0 mTorr
S $2p_{3/2}$	162.9	162.2	161.9
S $2p_{1/2}$	164	163.4	164

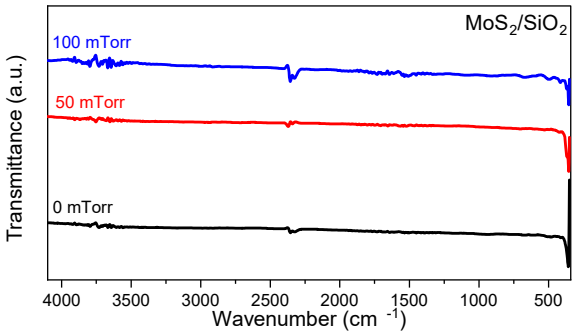

Fig. 7 – FTIR spectra of the deposition MoS_2 films by PLD on SiO_2/Si wafer fabricated using different deposition pressures.

that the exciton peaks are almost unchanged for the deposited MoS_2 films at 0–50 mTorr. This behavior was clearly elucidated from the AFM images, leading to the change in the crystallinity of nanoparticles at different deposition pressures. As the deposition pressure increases, the PL intensity signal is significantly affected owing to the change in the order–disorder structural degree of MoS_2 films and the localized states in the band gap will occur at higher wavelength. However, a low PL emission develops with a red-shift wavelength in the NIR regime. This is mainly owing to the scattering of MoS_2 species with Ar-gas atoms for the film grown at 100 mTorr. Thereupon, the crystalline structure quality of MoS_2 is influenced, leading to the change in the stoichiometry and occurrence of low S vacancies in the films comparatively to the samples produced at 0 mTorr. The low PL amplitude revealed the insignificant recombination of the electron–hole pairs and the red emission is attributed to the deep defects. Thus, the electrons will simply attain the surface films, inhibiting the direct recombination of charge carriers. As the buffer Ar-gas pressure increases, a deceleration in the kinetic energy appeared for the ablated particles and the scattering of ablated Mo and S atomic species will rise. Therefore, the particles number will be reduced when reaching the substrate surface since the gas molecules number is greater than the ablated particles number. The existence of buffer Ar-gas environment affects also the expansion dynamics of the plasma. Conversely, the deposited films at 0 and 50 mTorr, have intense emission peaks in the visible regime revealing the charge carriers recombination. Therefore, the intense PL peaks associated to the excitonic emission are indicated by the recombination of valence band (VB)—conduction band (CB) and the electron–hole pair separation may be increased in the Vis regime for these films. The PL spectra variation would also be attributed to the charge transfer modification between MoS_2 films and SiO_2 surface in terms of excitonic emission features under various deposition pressures. The intensity of PL features for the layered MoS_2 films on wafer substrates, can be influenced from the existing of extra non-radiative pathways for the recombined exciton, like the process of charge transfer and the dipolar–dipolar interactions. Moreover, it is well recognized that SiO_2 substrates can diminish the intensity of the PL emission via the scattering

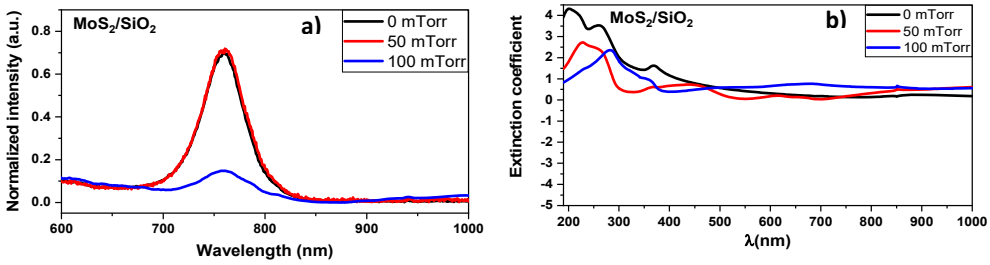

Fig. 8 – (a) Photoluminescence spectra of as-grown MoS_2 samples and (b) Extinction coefficients of MoS_2 films fabricated using different deposition pressures.

and interference phenomena with the optical phonons of the surface [22,46,60–62].

3.4.2. *Extinction coefficient*

The extinction coefficient reveals the viability of light penetration into a material at a certain wavelength and it also describes the absorption of light radiation. Fig. 8(b) displays the extinction coefficient of MoS_2 films synthesized under various deposition pressures. It is well noticed that MoS_2 films possess two separated exciton peaks around 320 nm and 385 nm for the sample prepared at 0 mTorr (see Fig. 8(b)), revealing the favorable light absorption comparatively to MoS_2 films prepared at elevated deposition pressures. Extinction is associated with the transmittance, as displayed in Fig. 8(b). Plots of the optical extinction spectra illustrate also several characteristic peaks located at 290, 310, and 340 nm for the MoS_2 films synthesized at 0, 50, and 100 mTorr, respectively. The outcome drawn from the extinction curves of the synthesized samples at elevated deposition pressures, is owing to the light absorption in the visible window. This can be reflected to the alteration of defective states into other energetic states. This behavior corresponds to the power law for the background of non-resonant scattering higher than 720 nm in these samples. All films spectra exhibit excitons around 385, 361, and 358 nm, respectively, corresponding to deposition pressures of 0, 50, and 100 mTorr, respectively. Furthermore, the dispersion of extinction spectra relies on the variation of the stoichiometry of films and aggregates size at low and high deposition pressures. It is well distinguished that the extinction coefficient displays a feature peak ~690 nm at higher deposited pressure. This is an indication of the high absorption of light at low wavelength in MoS_2 films. However, the extinction coefficient is insignificant in MoS_2 films, prepared in the vacuum pressure. This can be reflected to a transparent material at wavelength above 690 nm and an attenuated intensity is noticed at elevated wavelengths. When the deposition pressure varies, the generation of charge carriers that occurred on the substrate surface may tailor the band gap of MoS_2 films. Also, the deposition gas pressure affects significantly the expansion of laser-generated plasma due to the interaction of the ablated species with the gas molecules. The low intensity of first peak of MoS_2 film synthesized at 50–100 mTorr is attributed to the presence of low S-deficiency and to the decrease of incident particles on the substrate surface. It was also inferred that the quantum confinement in the layered Mo 4d-electron material is significant irrespective to those determined in sp-bonded semiconductor nanostructures [47–51].

3.4.3. *Absorbance spectra*

The deposition pressure effects on the light absorption of MoS_2 films are characterized via UV–Vis–NIR spectroscopic technique. As apparent from Fig. 9, the absorption pursues an analogous tendency like the extinction coefficient up to the incident radiation energy around 4.27 eV. For the incident light possessing a photon energy bigger than 4.27 eV, the enhancement in the absorption spectra occurs even for a reduced extinction coefficient behavior. The UV–Vis–NIR absorption spectrum of MoS_2 films (0 mTorr) exhibits a visible wide peak positioned at 332 nm, which ascertains the excitonic character of MoS_2 nanosheets. The sample prepared at 100 mTorr deposition pressure, possesses a wide optical gap (2.85 eV) in the blue shift range. Also, features are assigned to two excitons of wavelengths ~600 and 830 nm that split by 130 nm because of the spin–orbit splitting and interlayer interaction. Clearly, these two broad peak positions exhibit a red-shift in the MoS_2 films. The absorption spectra of all three samples illustrate shoulders altering between 350 nm and 750 nm, which are ascribed to the inter-band transitions arising from the Mo-4d to S-3p states. The two samples prepared at higher deposition pressures display six typical peaks, respectively at 50 mTorr (349, 591 and 745 nm), and 100 mTorr (332, 435 and 830 nm) corresponding to the characteristic absorption band in the MoS_2 films. The feature peaks located around 745 and 830 nm are assigned to the K point of the Brillouin zone [3,22,51]. However, the feature peaks positioned around 349 and 435 nm, are related to the direct transition arising from the valence states to the conduction states of

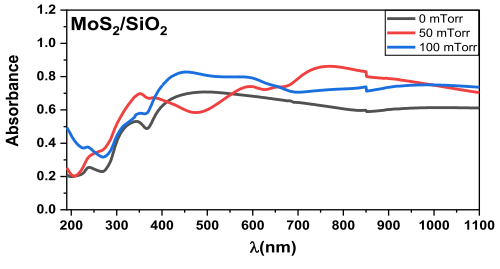

Fig. 9 – Absorbance spectra of MoS_2 films fabricated using different deposition pressures.

MoS_2 films. A typical peak is noticeable in the near-UV span (less than 300 nm) corresponding to the excitonic behavior of MoS_2. For the film prepared in the vacuum, the optical band gap assigned to the substantial peak of the optical absorbance, is owing to the presence of defects in it. Therefore, the defects will be diminished and the optical band energy is decreased at higher deposition pressure. At Ar-gas pressure of 50 mtorr, a red shift occurs in the optical band gap of the synthesized MoS_2 film, which takes place in NIR or far-infrared regimes of the electromagnetic spectrum. The increased RMS surface roughness in the laser ablated MoS_2 film prepared at 0 mTorr will also participate to increasing the optical band gap. Therefore, the optical band gaps of the MoS_2 films are somehow affected as the buffer Ar-gas pressure increases and thereby the S vacancies reduce in the chamber over the deposition process. Importantly, the buffer gas-pressure renders the ejected species to be decelerated in the plasma, owing the interaction of the species that strike the molecules of the gas. The buffer Ar-gas pressure affects significantly the quality of crystalline growth of MoS_2 films. The high absorption in MoS_2 films prepared at deposition pressure of 0 mTorr is attributed to the deposition rate, as exhibited by AFM observation. A pronounced blue shift wavelength (~460 nm) is detected in the MoS_2 films prepared at elevated deposition pressures. It was reported that the occurrence of significant blue shift wavelength in the optical absorption is assigned to the quantum confinement effects when the lateral size is diminished for the MoS_2 nanosheets. The presence of Mo–S bond character in all sample was further assigned via FTIR spectra. The marginal peak at 450 cm^{-1} is accredited to the Mo–S vibrational mode of MoS_2 films, while the band positioned around 750 cm^{-1} matches with Mo–O vibrational modes. This can reveal the coexistence of sulfides and oxides in the prepared films at various deposition pressures. Our results exhibit that MoS_2 films would be beneficial for the detection of light in the visible span (lesser than 500 nm) for photodetectors applications, owing to their sensibility to the wavelength of 450 nm.

3.5. *First principles calculations*

3.5.1. *Electronic properties*

The computational modellings based on density functional theory calculations are very useful to elucidate the experimental results and to predict the properties of new complex materials [22–25]. In this regard, we executed first principles calculations based on pseudopotential method to compute the electronic and optical properties of pristine and vacancy point-defective in MoS_2 monolayer. The Vienna ab initio simulation package (VASP) is employed for this purpose [65]. The basis set of plane-wave involving inner fixed core states, is employed for the electronic structure calculations within projector augmented wave (PAW) approach [66]. A generalized gradient approximation (GGA) for the exchange correlation functional was used, in terms of Perdew, Burke and Ernzerhof (PBE) approach [67]. For the calculations of electronic properties of all systems, HSE06 scheme is used for both pristine and vacancy defects in 2H–MoS_2 monolayers. A15 × 15 × 1 dense mesh was selected for the calculations of optical properties. To ensure a better convergence for the total energy less than 1 meV/atom, the plane-wave energy cutoff of 390 eV as well as sufficient fine grid of fast Fourier transformation relying on the supercell are employed. For the optimization of structural geometries and electronic structures of the pure and sulfur vacancy defective in MoS_2 monolayers, the criteria of convergence of 1.0×10^{-4} eV/Å and 1.0×10^{-6} eV/cell, is selected by involving the total relaxation of shape and cell size for the overall atomic coordinates, respectively, in order to acquire reliable results. A 3 × 3 × 1 supercell for the MoS_2 monolayer is constructed to create mono-vacancy and di-vacancy of sulfur atoms. In order to prevent the important slab interactions, a vacuum of 17 Å is involved. The generation of 15 × 15 × 1 k-mesh of **k**-point sampling is established by employing the Monkhorst–Pack technique [68]. The relaxation of all atomic positions are achieved in the plane and the vertical positions are persevered unchanged.

The optimization of the structural parameters are performed for the hexagonal lattice MoS_2 after minimizing the total energy versus the cell lattice. Then, the outcome equilibrium structural lattice parameters $a_0 = 3.184$ Å and $c_0 = 12.97$ Å are determined, which are in line with the earlier theoretical and experimental works [20–22,56]. The space group $P6_3/mmc$ is referred to the unit cell of MoS_2 bulk which is composed of 6 atoms (2 Mo and 4 S). Here, the stacking of MoS_2 layers is settled along c-direction of the unit cell of 2H–MoS_2. This is owing to the neglecting of Van der Waals interaction between MoS_2 layers along c-direction, analogous to graphene-type hexagonal order. To acquire a covalent bonding for MoS_2 sheet, the coordination of each Mo atom is connected to six S atoms at both lower and upper sides of layers (c-direction) in a pattern of triangular prismatic. Also, the bonding of each sulfur atom is made in c-direction with three Mo atoms and bonded to six sulfur atoms in the basal plane to acquire a hexagonal order. The interatomic distance of Mo–S is about 2.41 Å (Fig. 10). All the computed properties are executed for the free-standing MoS_2 single-layer by generating a 3 × 3 × 1 supercell, as depicted in Fig. 10. As typical point defects, the attachment of a single S vacancy (V-S) and divacancies (V-S_2) of two sulfur atoms (one atom at the upper layer and the other one at the lower side of MoS_2 layer) are indicated for the same Mo atom (see Fig. 10). Illustrative structural geometrical models for 2H–MoS_2 monolayers with 3 × 3 × 1 supercell are displayed in Fig. 10 (b) and (c), involving both V-S and V-S_2 point defects.

To assist the experimental determinations, we examined the electronic features, such as the band structures, and density of states (DOS) of perfect MoS_2 monolayer and defective structures with the alteration of sulfur vacancies (as sulfur and two sulfurs point defect species) in the host 2D-material. In our investigation, solely neutral point defects are introduced for simplicity. The electronic band structures of defect-free MoS_2-monolayer compared to the defective monolayers comprising V-S and V-S_2 vacancies, are displayed in Fig. 10(a)–(c). Also, the inspection of DOS can be elucidated immediately via the electronic band structure curve of free-defect MoS_2 sheet, as displayed in Fig. 10(a). The optimized structure of MoS_2 single layer has a semiconductor behavior with a direct band gap transition of 1.85 eV along Γ- Γ-direction of k points in the Brillouin zone (see Fig. 10(a)). The band structures of V-S into the host MoS_2 monolayer acquired localized defect states. It is noticeable that the defective states

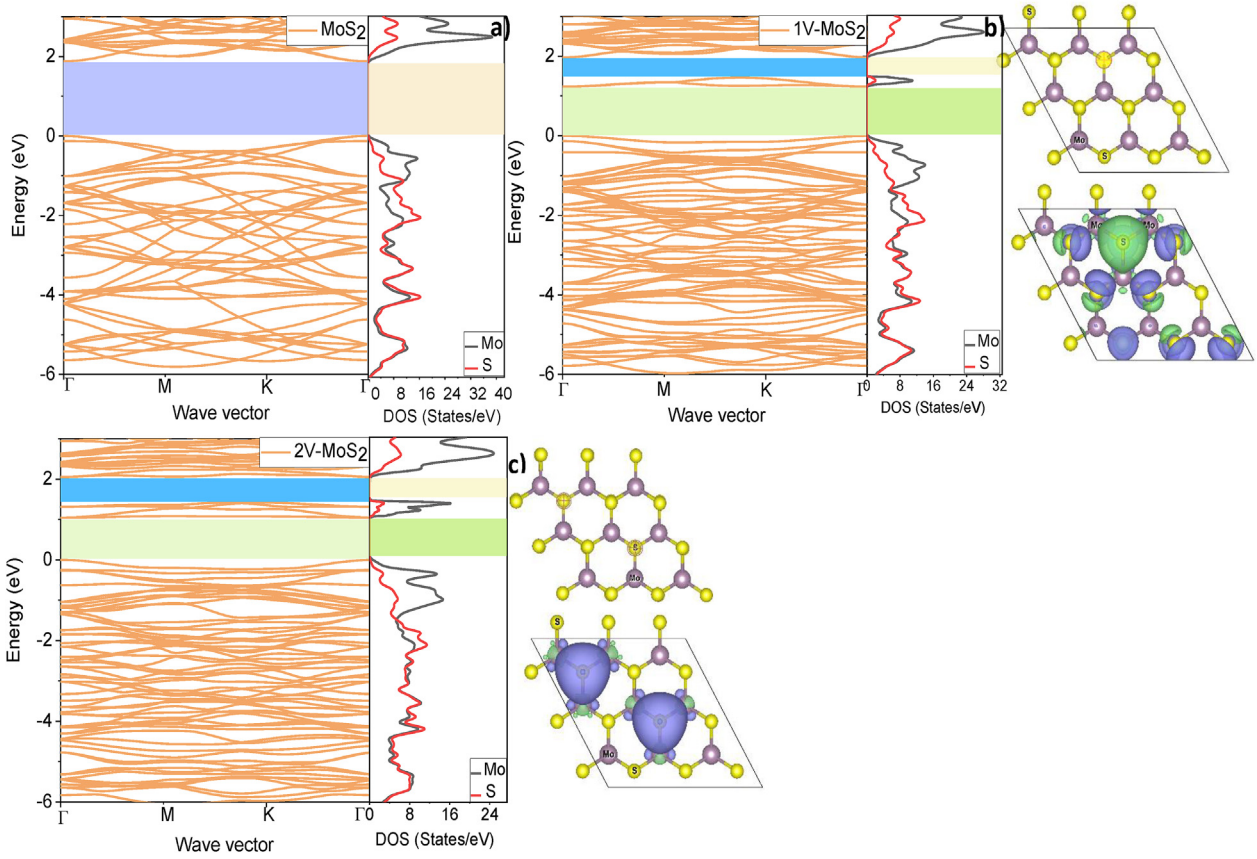

Fig. 10 – The hexagonal structural configurations of perfect 2H–MoS_2-single-layer with 3 × 3 × 1 supercell geometry, while (Mo atom are in purple, and S atom in yellow). In 2H–MoS_2-single-layer with 3 × 3 × 1 supercell geometry, one sulfur and two sulfurs are removed to create vacancy point defects, in both top and bottom sides of layer of MoS_2) by preserving the symmetry of the lattice, as portrayed in right sides (b) and (c). Simplified band structures for defect-free of 2H–MoS_2 3 × 3 × 1 supercell-sheet and native vacancy point defects, such as single-vacancy and di-vacancy of S atoms are indicated (a), (b), and (c) along with their charge density difference around the sulfur vacancies. The electronic structures display impurity states at the mid-gap for V-S and V-S_2 anion atoms in the host MoS_2-single layer, yielding a narrow band gap systems. The perfect MoS_2 single-layer displays a semiconducting character with a direct band gap of 1.85 eV between the lower conduction states and the uppermost valence states, owing to the zone-folding over the Γ- Γ-direction of k points in the Brillouin zone. In (b) and (c), the density of states are modified by the introduction of S-V and S-V_2 in MoS_2 single-layer comparatively to the pure defect-free MoS_2 sheet. The feature peaks emerge between the upper valence states and lower conduction states confined between green and yellow areas.

are located at mid-gap above the upper valence sates in MoS_2-monolayers containing both single-vacancy and divacancy of S atoms. For single-vacancy of S atom, the V-S defective states in MoS_2 sheet are located near the lower conduction with a band gap reduction. Conversely, the V-S_2 defective states are located at the midgap, arising into the band gap depression. It is remarkable that the number of defective subbands rises when the number of S-vacancy increases in MoS_2 single-layer. The dispersion of electronic band structures plots display a band folding multiple times for any vacant point defect species. However, the band gap is reduced comparatively to the defect-free MoS_2 sheet and the midgap defective states are significantly localized because of the hybridization between Mo-4d and S-3p orbitals. These states turned fully into dispersionless and flatness that are located in the bandgap. This is owing to the weakening of covalent character of Mo–S bonding near the S-vacancy position. Also, the midgap between Γ- Γ direction is positioned around 1.4 and 1.2 eV for the defective monolayers with V-S and V-S_2 vacancies, respectively. The vacancy defects tailor the band gap, while the subbands number increases at the mid-bandgap with the increase of S-vacancy in MoS_2 sheets.

To trace the evolution of both electronic structures of perfect and defective monolayers MoS_2, we computed their projected density of states (PDOSs) on Mo and S atoms, as portrayed in Fig. 10(a)–(c). From the analysis of PDOS plots, the S-p-orbitals of defective atoms are subject to the feature peaks of upper valence states that are responsible in the formation of electronic states nearby Fermi-state. In correspondence with the band-structure dispersion curve, the band-gap acquired from the DOS is about 1.85 eV for the perfect MoS_2 sheet (see Fig. 10(a)). It is clearly noticed that the upper valence states and lower conduction states of defect-free MoS_2 single-layer are mainly formed of hybridized Mo 4 d and S 3p states,

leading to a strong covalent character of Mo–S bond. For S mono/di-vacancies into MoS_2 sheets, many impurity levels arise in the mid-band gap (see Fig. 10(b) and (c)). These impurity levels are composed of hybridized Mo 4 d and S 3p states, and become delocalized when S-vacancy number increases. This will rise the participation of Mo-3d states in the DOS of V-S_2 structure with the increased number of non-terminated bonds of the defected S atoms comparatively to its perfect structure. The total spectral peaks of the lower conduction states of Mo/S atoms included in the pure MoS_2 sheet, are altered in both V-S and V-S_2 defective structures. For the V-S structure, the first peak sets contain principally S-3p states which are owing to the dangling bonds of the neighbors of S atoms, developed from the lower valence states, although both Mo-4d and S-3p arising from the second and third peak sets are quite unchangeable (−5.7 to −3 eV) (see Fig. 10(b)). As displayed in Fig. 10(c), the spectral peaks of DOS of V-S_2 structure nearby Fermi level became narrow. The Mo-4d-orbitals are responsible for the participation of lower conduction states and upper valence states, while the S-3p-orbitals reveal a weak peak in the conduction states ~1 eV. For S-divacancy inserted into MoS_2 layered structure, the defective states relocate toward the conduction states, inferring a p-type semiconducting nature. Whilst the localized midgap states may significantly impact the electron transport of 2D material, these defective states are dominant for the enhancement in the photoluminescence intensity [36,39,56–63].

For the purpose to inspect the change in the chemical bonding of defective monolayers, the charge density differences of the first neighbors around the Mo–S bonding at S-mono-vacancy and S-divacancy defects in MoS_2 single layers, are plotted in Figs. 10(b) and (c). The calculated charge density difference is acquired from the electron densities of monolayer MoS_2, Mo atoms, and S atoms, respectively. The charge redistribution is formed from the vacancy point defect, although the modification in the electron density is owing to the atomic bonding. Note that the S and Mo atoms located below and above the purple zone, exhibit an increase in the electron density nearby the S-divacancy defects. The green area illustrates the electron density loss after the bonding. The significant charge transfer arising from S-monovacancy is the outcome of significant interaction between the vacancy sites and Mo stemming in the highly stabilized system. It is revealed that Mo–S bonding gives arise to a covalent nature around the single vacancy of S atom and edge atomic sites between Mo–S bonding in MoS_2 monolayer. Note that the increase in S-vacancy concentration, induces a weakening of Mo–S bonding caused by V-S_2 type defect. Subsequently, the charge density difference reduces with the augmentation in S-vacancy concentration, inferring a weakened covalent bonding behavior of Mo–S (Fig. 10). This can simply due to the reduction in the ionic bonding character of defective monolayer MoS_2. Thus, the generation of dangling bonds happened around Mo atoms when the S-vacancies type defects are present in MoS_2 monolayer. This would conduct to the modification in bond-lengths around the vacancy point defects. In a defect-free structure, the bonding of each sulfur atom that possesses two valence electrons is connected with two molybdenum electrons. Hence, for the missing of sulfur atom, these two molybdenum electrons became unsaturated, referring to the neutral state of the typical point defect. For both V-S and V-S_2 typical defects, the distribution of charge is shared between Mo and S atoms, surrounding the point defect (see Fig. 10). Accordingly, the modifications of the confined charge occurs at the nearest atomic sites around S atoms for V-S point defect. Conversely, the change in the charge is remarkable for V-S_2 defect close to the first-neighbor and second-neighbors of Mo atomic sites. This can be attributed to the more delocalization behavior of Mo-4d orbitals irrespective to S-3p orbitals.

3.5.2. *Optical properties*

The frequency-dependence dielectric property corresponding to incident photons, characterizes the optical aspects of materials that can be computed on the basis of self-consistent charge density. The estimated dielectric response dependent on frequency, is associated with the large number of vacant states to enable wider interval of interband excitations between the valence states and conduction states. By this way, it is feasible to establish better results for the optical properties of the systems under study. The key factor, such as the complex dielectric function is divided into two terms, which are the real and imaginary components for providing reliable information about the optical properties of a material. Then, $\varepsilon(\omega) = \varepsilon_1(\omega) + i\varepsilon_2(\omega)$ is formulated via the material response to the light spectrum. On the basis of optical spectra of incident radiation represented by the real and imaginary expressions of $\varepsilon(\omega)$, the absorption coefficient, and energy loss function can be extracted [37].

To gain a better knowledge about the optical behaviors of V-S and V-S_2 vacancy point defects involved into the free-standing MoS_2 monolayer with hexagonal symmetry, their optical absorption coefficients ($\alpha(\omega)$) are systematically analyzed. The optical spectra of pristine MoS_2 monolayer, V-S-MoS_2, and V-S_2-MoS_2 defective monolayers are computed along both polarization vectors of light for $E_{\parallel}$ (in a-b-plane) and $E_{\perp}$ (out-of-plane). They are indicated by $\alpha^{\parallel}(\omega)$ and $\alpha^{\perp}(\omega)$ components at photon energy range of 0–20 eV. First of all, the spectral features of $\alpha^{\parallel}(\omega)$ curves are intense irrespective to that of $\alpha^{\perp}(\omega)$ component, manifesting an anisotropic trend at the lower photon energy interval for this 2D crystal structure without and with points defects. As clearly seen from Fig. 11, the absorption edge starts around 1.97, 1.6, and 1.3 eV, respectively, for the pristine MoS_2 monolayer, V-S-MoS_2, and V-S_2-MoS_2 defective monolayers, revealing the optical band gap (Egopt) along with the global solar spectrum (AM1.5G) of incident light on the earth. The AM1.5G incorporates the direct and diffusing rays of light arising from the sun that is utilized as references for photovoltaic materials [5]. The threshold of optical absorption coefficient exhibits an alteration from the blue shift to the red shift of the solar spectrum regime and the solar irradiance is displayed in radish color. It is well noticed that the optical absorption coefficient spectra $\alpha^{\parallel}(\omega)$ and $\alpha^{\perp}(\omega)$ have an anisotropic shapes for all systems at photon energies below 13 eV, and thereafter their patters turn into isotropic profile upward 13 eV, as depicted in Fig. 11. Also, the first spectral peaks are the signature of electron transitions between the valence bands of S 3p states and conduction bands of Mo 4 d states. Secondly, $\alpha^{\parallel}(\omega)$ and $\alpha^{\perp}(\omega)$ components

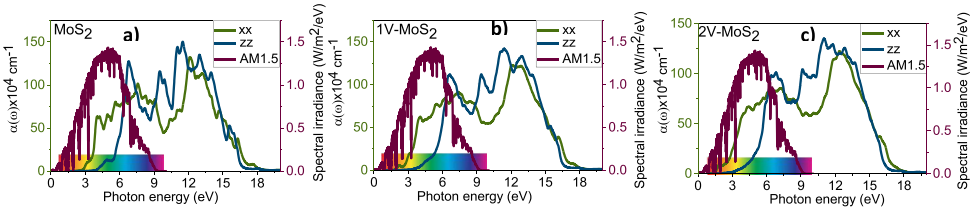

Fig. 11 – Calculated in-plane and out-of-plane of optical absorption coefficient of (a) free-defect 2H–MoS_2 3 × 3 × 1 supercell – monolayer, (b) V-S, and (c)V-S_2 as a function of photon energy. Green and blue curves correspond to basal-plane and out-of-plane polarization of incident photons, respectively.

of the optical absorption coefficients exhibit analogous trends for defective monolayers except for the threshold value. Thirdly, the main spectral peaks are located below 13.5 eV, while the optical spectra curves are almost unchanged at higher energy regime. The second remarkable peak of $\alpha^{\|}(\omega)$ occurs around 3.1 eV corresponding to the energy located in the midsection of Γ-M k-points for V-S defective monolayer. A noticeable spectral peak is detected at 6.3 eV in the out-of-plane spectrum for V-S point defect in MoS_2 monolayer. It is well noticed that a low peak occurs at 1.4 eV related to the excitation arising from the filled valence states to conduction states. Also, the spectral peaks emerge at 1.85 and 1.4 eV for V-S and V-S_2 point defects in MoS_2 monolayer that can be reflected to the excitation via the defective filled states. The first broad spectral peaks emerged in the defective MoS_2 monolayers, are owing to the valence band around the mid-gap impurity level. Specifically, the appearance of a shoulder in $\alpha^{\|}(\omega)$ around 3.3 eV is associated with the occupied valence states to the empty defective levels, which are developed from the transition of S 3p states to Mo 4 d conduction states in both V-S and V-S_2 defective monolayers. The optical absorption spectra of $\alpha^{\|}(\omega)$ and $\alpha^{\perp}(\omega)$ components for defective monolayers have a quite analogous dispersed spectral at higher frequencies (as noticed in Fig. 11). The absorption in a-b plane polarization of defective monolayers vanishes in the regime of 9–12 eV since the energy of incident photons is minor (Fig. 11). Both $\alpha^{\|}(\omega)$ and $\alpha^{\perp}(\omega)$ profiles are almost unchanged in the light energy regime ~ 15.5–19.5 eV. For both mono/divacancy defective monolayers, the absorption spectral peaks shifts systematically to the lower light energy comparatively to the defect-free case. The augmentation of S vacancy contents in the MoS_2 sheet, yields the material to have impurity levels developing a significant light absorption from the visible to the NIR span. Hereafter, the optical absorption profiles display a redshift with a reduced band gap referred to the solar cell irradiance spectrum. Furthermore, several extra spectral peaks are detected at low photon energy in the defective MoS_2 monolayers with enhanced optical absorption spectra when S vacancy content increases. This assumes that the dependence on the vacancy type-defect, such as the atomic defects in MoS_2 monolayers render them compelling candidates in the sunlight absorbers with an enhancement of solar cells efficiency in photovoltaic systems [44,48,60–62].

Electron energy loss function spectra provide a guidance about the interband transitions of single electron that can be discerned at low energy range from the oscillations of collective plasma [18]. This may characterize the loss of electrons, traveling along a uniform dielectric medium. The electron energy loss function $L(\omega)$, contains two parts, the first one is in a-b-plane ($L(\omega)\|$) (over a- and b-axis) and the second one is out-of-plane ($L(\omega)\perp$) (over c-axis). The energy loss function of intrinsic MoS_2 monolayer and S-vacancy defective monolayers are displayed in Fig. 12. Three major energy loss peaks occur in L (ω) spectra owing to the resonance frequency of plasma ω_p. The position of energy loss peaks are associated with the critical points, while the material transitions take place from dielectric to metal. In the case of sulfur mono- and divacancies into MoS_2 monolayers, the beginning energy loss peak is insignificant at low radiation energy irrespective to the perfect MoS_2 single layer, while the plasmon peak in the loss function occurs about 7.8 and 6.6 eV for the polarizations in a-b-plane and out of plane. It is noticeable that the first plasmon peaks in $L(\omega)\|$ are reduced and relocated to 6.3 and 6.0 eV for V-S and V-S_2 vacancies in MoS_2 monolayers. As illustrated in Fig. 12, the second marked sharp peaks in energy loss spectra are centered between 12 and 15 eV for both $L(\omega)\|$ and $L(\omega)\perp$ of all MoS_2 monolayers. A substantial anisotropic trend emerges for free-defect and defective monolayers at the same light photon energy span. Thus, the loss energy behavior disappear approximately around the radiation energy regime of

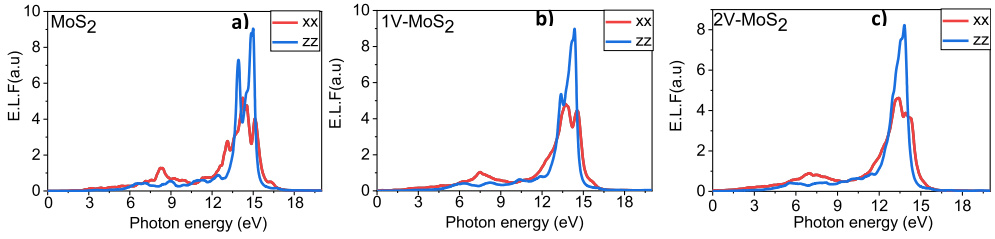

Fig. 12 – Energy loss function of (a) free-defect 2H–MoS_2 3 × 3 supercell – monolayer, (b) V-S, and (c) V-S_2 as a function of photon energy. Red and blue curves correspond to basal-plane and out-of-plane polarization of incident photons, respectively.

16–17 eV. It is well noticeable that the electron energy loss function displaces to the lower energy when S-vacancy increases in MoS_2 monolayer. The electron energy loss function describes the decomposition of two significant resonance characteristics for defect-free MoS_2 in basal plane polarization (E⊥c) located below 9.1 eV because of π plasmons (π-π* transitions) and upward 9.1 eV is owing to π+σ plasmons (σ- σ* as well as π-σ* transitions) (see Fig. 12). For polarization perpendicular to a-b plane (E||c) the solely resonance characteristics is upward 9.5 eV, arising from significant σ- σ* and π-σ* transitions. Note that MoS_2 possesses 18 valence electrons. Hence, the Mo–S strong bonding is composed of 12 electrons/molecule with mixtures of s, p, and d states that stem into the σ valence states, although the rest six electrons are subject to the π-plasmon states. The two filled states containing the d_{z2} orbitals of the metal atom are among the six electrons in the π-plasmon states that displace marginally. Therefore, the substantial red-shift can be detected in the π+σ plasmon peaks for both $L(\omega)\|$ and $L(\omega)\perp$when altering from the defect-free to the vacancy defective monolayers with the increase of S-vacancy content. It is inferred that the incident electrons of various energies take place on the surface of MoS_2, while the loss of energy cropped up more conveniently at the vacancy sites because of elastic collision with electrons between 8 and 9 eV. The peak signal in the defective monolayer is minor comparatively to the intrinsic MoS_2 monolayer. Hence, the energy loss of electron traversing the defective monolayer is sluggish, which has a redshift nature.

4. Conclusion

In summary, the synthesis of MoS_2 films on SiO_2/Si substrates were successfully achieved within the PLD technique under different buffer Ar-gas pressures at substrate temperature of 700 °C. In this respect, the structural, morphological, and optical properties of these films were inspected employing various characterization tools. Our experimental measurements revealed the influence of buffer Ar-gas pressure on the morphology surface, and optical behaviors of MoS_2 films grown on SiO_2/Si substrate. Accordingly, this can affect the interaction variation between the laser-ablated MoS_2 films and SiO_2/Si substrate surface The SEM characterizations revealed that the deposited MoS_2 films possess hexagonal crystallinity domains. Therefore, the buffer Ar-gas pressure variation influences significantly the surface morphology of the deposited films, while a quasi-uniformed dense distribution of crystallites was obtained for the synthesized films at 0 mTorr. XRD patterns exhibited a 2H-phase for MoS_2 films, as divulged from (002) facet. Also, the AFM analysis indicated a systematic reduction in the thickness of films versus the increased buffer Ar-gas pressure. The UV–vis–NIR and FTIR spectra revealed the occurrence of Mo–S as well as Mo–O bonds in the films. As apparent from XPS, the S-deficiencies represent the preferential positions for Van der Waals interaction with low density of defects. The PL spectroscopy illustrated emission bands spanning in the Vis-NIR regimes with the signature of charge transfer between MoS_2 films and SiO_2 surface via the inspection of excitonic emission features. Subsequently, the formation of films illustrated a decrease in the intensity of PL peak with the increase of deposition pressure. A red-shift is detected in the optical gap versus the increase of buffer Ar-gas pressure in the chamber during the deposition process. This is essentially owing to the smoothness of surface morphology and thereby sulfur vacancies will be diminished in these films. Using first-principles calculations, the electronic band structure and density of states outcomes illustrated that the perfect MoS_2 monolayer has a semiconductor behavior with a direct band gap transition. Interestingly, it was unveiled that the increased compositional sulfur-vacancy defects in MoS_2 single-layer created impurity levels at the mid-band gap above the upper valence states, leading to an acceptor type character with a reduced band gap. For defective vacancies in MoS_2 monolayers, the optical spectra profiles of polarization in-plane revealed extra spectral peaks at lower photon energy regime versus the increase of sulfur vacancy content in MoS_2 monolayer. Furthermore, the localized mid-gap states represent a significant property for the activation of new optical transitions altering from the visible to NIR spans of incident photon energy below the band-gap of defect-free 2D-structures. A pronounced plasmon peak in the energy loss function was relocated to the lower photon energy versus the increase of sulfur vacancy defects. Our investigation would be informative for future design of optoelectronic devices based on PLD-synthesized MoS_2 films under the effect of buffer Ar-gas pressure. It is therefore expected that our experimental and theoretical outcomes will afford promising functionalities, such as the generation of light emission in the defective layered MoS_2 materials. This will eventually give rise to desired optical transitions suitable for higher efficiency of photovoltaic devices, solar cell window layer, infrared detectors, and light emitting diodes.

Declaration of Competing Interest

The authors declare that they have no known competing financial interests or personal relationships that could have appeared to influence the work reported in this paper.

Acknowledgment

This research project was supported by a grant from the "Research Center of the Female Scientific and Medical Colleges", Deanship of Scientific Research, King Saud University.

REFERENCES

[1] Khan Karim, Khan Tareen Ayesha, Aslam Muhammad, Wang Renheng, Zhang Yupeng, Mahmood Asif, et al. J Mater Chem C 2020;8:387–440.
[2] Cheng Jinbing, Wang Chunlan, Zou Xuming, Liao Lei. Adv Opt Mater 2018;7:1800441.
[3] Soleimani-Amiri Samaneh, Gholami Rudi Somayeh. Opt Mater 2020;110:110491.
[4] Cao X, Tan C, Zhang X, Zhao W, Zhang H. Solution-processed two-dimensional metal dichalcogenide-based nanomaterials for energy storage and conversion. Adv Mater 2016;28:6167–96.

[5] Manzeli Sajedeh, Ovchinnikov Dmitry, Pasquier Diego, Yazyev Oleg, Kis Andras. Nature Rev Mater 2017;2:17033.
[6] Ansari N, Mohebbi E, Fallah K. Opt Mater 2020;107:110039.
[7] Mak KF, Shan J. Photonics and optoelectronics of 2D semiconductor transition metal dichalcogenides. Nat Photonics 2016;10:216–26.
[8] Choi Wonbong, Choudhary Nitin, Han Gang Hee, Park Juhong, Akinwande Deji, Hee Lee Young. Mater Today 2017;20:116–30.
[9] Chu XS, Yousaf A, Li DO, Tang AA, Debnath A, Ma Duo, et al. Chem Mater 2016;30:2112–28.
[10] Abd Malek Nurul Ain, Alias Nabilah, Md Saad Siti Khatijah, Abdullah Nur Adliha, Zhang Xin, Li Xiaoguo, et al. Opt Mater 2020;104:109933.
[11] Xiao Li, Zhu Hongwei. Journal of Materiomics 2015;1:33–4.
[12] Chakraborty Biswanath, Bera Achintya, Muthu DVS, Bhowmick Somnath, Waghmare UV, Sood AK. Phys Rev B Condens Matter Mater Phy 2012;85(16):161403.
[13] Zhang Long, Wan Langhui, Yu Yunjin, Wang Bin, Xu Fuming, Wei Yadong, et al. J Phys Chem C 2015;119:22164–71.
[14] Nayeri Maryam, Fathipour Morteza. Analytical study of the electronic and optical properties of the armchair MoS2 nanoribbons. Phys B Condens Matter 2020;594:412337.
[15] Fadaie M, Shahtahmassebi N, Roknabad MR, Gulseren O. Phys Lett A 2018;382:180–5.
[16] Lee C, Wei X, Kysar JW, Hone J. Science 2008;321:385–8.
[17] Salehi Saboura, Saffarzadeh Alireza. Surf Sci 2016;651:215–21.
[18] Friedman AL, Perkins FK, Hanbicki AT, Culbertson JC, Campbell PM. Nanoscale 2016;8:11445–53.
[19] Hieu Nguyen N, Ilyasov Victor V, Vu Tuan V, Poklonski Nikolai A, Phuc Huynh V, Le Thi Thu Phuong, et al. Superlattice Microst 2018;115:10–8.
[20] Gokhan Sensoy Mehmet, Vinichenko Dmitry, Chen Wei, Friend Cynthia M, Kaxiras Efthimios. Phys Rev B 2017;95:014106.
[21] Liu Mengxi, Shi Jianping, Li Yuanchang, Zhou Xiebo, Ma Donglin, Qi Yua, et al. Small 2017;13:1602967.
[22] Kuate Defo Rodrich, Fang Shiang, Shirodkar Sharmila N, Tritsaris Georgios A, Dimoulas Athanasios, Kaxiras Efthimios. Phys Rev B 2016;94:155310.
[23] Feng Li-ping, Sun Han-qing, Ao Li, Jie Su, Yan Zhang, Zheng-tang Liu. Mater Chem Phys 2018;209:146–51.
[24] Jie Wenjing, Hao Jianhua. Nanoscale 2018;10:328–35.
[25] McMorrow Julian J, Cress Cory D, Arnold Heather N, Sangwan Vinod Kumar, Jariwala Deep, Schmucker Scott W, et al. Appl Phys Lett 2017;110:073102.
[26] Jie Wenjing, Yang Zhibin, Zhang Fan, Bai Gongxun, Leung Chi Wah, Hao Jianhua. ACS Nano 2017;11(7):6950–8.
[27] Yang Zhibin, Jie Wenjing, Hin Mak Chun, Lin Shenghuang, Lin Huihong, Yang Xianfeng, et al. ACS Nano 2017;11(4):4225–36.
[28] Wang Qing Hua, Kalantar-Zadeh Kourosh, Kis Andras, Coleman Jonathan N, Strano Michael S. Nat Nanotechnol 2012;7:699–712.
[29] Lin Z, Liu Y, Halim U, Ding M, Liu Y, Wang Y, et al. Nature 2018;562:254–8.
[30] Sørensen Signe G, Fuchtbauer Henrik G, Tuxen Anders K, Walton Alex S, Lauritsen Jeppe V. ACS Nano 2014;8(7):6788–96.
[31] Mahjouri-Samani Masoud, Tian Mengkun, Wang Kai, Boulesbaa Abdelaziz, Rouleau Christopher M, Puretzky Alexander A, et al. ACS Nano 2014;8(11):11567–75.
[32] Syari'ati A, Kumar S, Zahid A, Ali El Yumin A, Ye J, Rudolf P. Chem Commun (Camb). 2019;55:10384–7.
[33] Bana Harsh, Travaglia Elisabetta, Bignardi Luca, Lacovig Paolo, Sanders Charlott E, Dendzik Maciej, et al. 2D Mater 2018;5(3):035012.
[34] Hall Joshua, Pielić Borna, Murray Clifford, Jolie Wouter, Wekking Tobias, Busse Carsten, et al. 2D Mater 2018;5:025005.
[35] Ma X, Shi M. Thermal evaporation deposition of few-layer MoS2 films. Nano-Micro Lett 2013;5:135–9.
[36] Baek SH, Choi Y, Choi W. Large-area growth of uniform single-layer MoS2 thin films by chemical vapor deposition. Nanoscale Res Lett 2015;10:388.
[37] Ansari N, Ghorbani F. J Opt Soc Am B 2018;35:1179–85.
[38] Conley Hiram J, Wang Bin, Ziegler Jed I, Haglund Jr Richard F, Pantelides Sokrates T, Bolotin Kirill I. Nano Lett 2013;13(8):3626–30.
[39] Cai Haifang, Guoa Yufeng, Gao Huajian, Guo Wanlin. Nanomater Energy 2019;56:33–9.
[40] Ling ZP, Yang R, Chai JW, Wang SJ, Leong WS, Tong Y, et al. Opt Express 2015;23:13580–6.
[41] Buscema Michele, Steele Gary A, Herre S, van der Zant J, Castellanos-Gomez Andres. Nano Research 2014;7(4):561–71.
[42] Loh Tamie AJ, Chua Daniel HC. ACS Appl Mater Interfaces 2014;6(18):15966–71.
[43] Serna Martha I, Yoo Seong H, Moreno Salvador, Xi Yang, Oviedo Juan Pablo, Choi Hyunjoo, et al. ACS Nano 2016;10(6):6054–61.
[44] Serrao Claudy R, Diamond Anthony M, Hsu Shang-Lin, You Long, Gadgil Sushant, Clarkson James, et al. Appl Phys Lett 2015;106(5):052101.
[45] Siegel Gene, Venkata Subbaiah YP, Prestgard Megan C, Tiwari Ashutosh. Apl Mater 2015;3(5):056103. M. Yi and C. Zhang, RSC Adv 8, (2018) 9564–9573.
[46] Tamie A J Loh, Chua Daniel HC, Wee Andrew TS. Sci Rep 2015;5:18116.
[47] Mahjouri-Samani Masoud, Ryan Gresback, Tian Mengkun, Wang Kai, Puretzky Alexander A, Rouleau Christopher M, et al. Adv Funct Mater 2014;24(40):6365–71.
[48] Salazar Norberto, Beinik Igor, Jeppe V, Lauritsen. Phys Chem Chem Phys 2017;19(21):14020–9.
[49] Grønborg Signe S, Ulstrup Søren, Bianchi Marco, Dendzik Maciej, Sanders Charlotte E, Lauritsen Jeppe V, et al. Langmuir 2015;31(35):9700–6.
[50] Liu Xiaolong, Balla Itamar, Bergeron Hadallia, Campbell Gavin P, Bedzyk Michael J, Hersam Mark C. ACS Nano 2015;10(1):1067–75.
[51] Zhang Chendong, Johnson Amber, Hsu Chang-Lung, Li Lain-Jong, Shih Chin-Kang. Nano Lett 2014;14(5):2443–7.
[52] Addou Rafik, Colombo Luigi, Robert M. ACS Appl Mater Interfaces 2015;7(22):11921–9.
[53] Hong Li, Tsai Charlie, Koh Ai Leen, Lili Cai, Contryman Alex W, Fragapane Alex H, et al. Nat Mater 2016;15:48.
[54] Le D, Rawal TB, Rahman TS. J Phys Chem C 2014;118(10):5346–51.
[55] Yasuda Satoshi, Takahashi Ryosuke, Osaka Ryo, Kumagai Ryota, Miyata Yasumitsu, Okada Susumu, et al. Small 2017;13(31):1700748.
[56] Pena-Alvarez Miriam, del Corro Elena, Morales-Garcia Angel, Kavan Ladislav, Kalbac Martin, Frank Otakar. Nano Lett 2015;15(5):3139–46.
[57] Shi Jianping, Ma Donglin, Han Gao-Feng, Yu Zhang, Ji Qingqing, Gao Teng, et al. ACS Nano 2014;8(10):10196–204.
[58] Dong L, Lou J, Shenoy VB. ACS Nano 2017;11:8242–8.
[59] Jariwala Deep, Sangwan Vinod K, Lauhon Lincoln J, Marks Tobin J, Hersam Mark C. ACS Nano 2014;8:1102–20.
[60] Dileep K, Sahu R, Sarkar Sumanta, Peter Sebastian C, Datta R. J Appl Phys 2016;119:114309.

[61] Tizei Luiz HG, Lin Yung-Chang, Mukai Masaki, Sawada Hidetaka, Lu Ang-Yu, Li Lain-Jong, et al. Phys Rev Lett 2015;114:107601.
[62] Roch Jonas Gael, Froehlicher Guillaume, Leisgang Nadine, Makk Peter, Watanabe Kenji, Taniguchi Takashi, et al. Nat Nanotechnol 2019;14(5):432–6.
[63] Yu Yifu, Nam Gwang-Hyeon, He Qiyuan, Wu Xue-Jun, Zhang Kang, Yang Zhenzhong, et al. Nat Chem 2018;10(6):638–43.
[64] Sahu R, Bhat U, Batra NM, Sharona H, Vishal B, Sarkar S, et al. J Appl Phys 2017;121(10):105101.
[65] Kresse GG, Furthmüller Jurgen. Phys Rev B Condens Matter 1996;54:11169.
[66] Blöchl PE. Phys Rev B Condens Matter Mater Phy 1994;50:17953.
[67] Perdew JP, Burke K, Ernzerhof M. Phys Rev Lett 1996;77:3865–8.
[68] Monkhorst HJ, Pack JD. Phys Rev B 1976;13:5188.